Journal of Physics: Condensed Matter

PAPER • OPEN ACCESS

Bulk and interface quantum states of electrons in multi-layer heterostructures with topological materials

To cite this article: Aleksandar Nikolic *et al* 2018 *J. Phys.: Condens. Matter* **30** 235001

View the article online for updates and enhancements.

Related content

- Topological materials
Binghai Yan and Shou-Cheng Zhang
- Topological phases in two-dimensional materials: a review
Yafei Ren, Zhenhua Qiao and Qian Niu
- Probing the wavefunction of the surface states in Bi2Se3 topological insulator: a realistic tight-binding approach
A Pertsova and C M Canali

IOP ebooks™

Bringing you innovative digital publishing with leading voices to create your essential collection of books in STEM research.

Start exploring the collection - download the first chapter of every title for free.

This content was downloaded from IP address 131.111.184.102 on 21/09/2018 at 13:30

OPEN ACCESS
IOP Publishing

Made open access 4 July 2018
Journal of Physics: Condensed Matter

J. Phys.: Condens. Matter **30** (2018) 235001 (15pp)
https://doi.org/10.1088/1361-648X/aac0b1

Bulk and interface quantum states of electrons in multi-layer heterostructures with topological materials

Aleksandar Nikolic[1], Kexin Zhang and C H W Barnes

Cavendish Laboratory, Department of Physics, University of Cambridge, Cambridge CB3 0HE, United Kingdom

E-mail: an340@cam.ac.uk

Received 16 January 2018, revised 2 April 2018
Accepted for publication 27 April 2018
Published 15 May 2018

Abstract

In this article we describe the bulk and interface quantum states of electrons in multi-layer heterostructures in one dimension, consisting of topological insulators (TIs) and topologically trivial materials. We use and extend an effective four-band continuum Hamiltonian by introducing position dependence to the eight material parameters of the Hamiltonian. We are able to demonstrate complete conduction-valence band mixing in the interface states. We find evidence for topological features of bulk states of multi-layer TI heterostructures, as well as demonstrating both complete and incomplete conduction-valence band inversion at different bulk state energies. We show that the linear k_z terms in the low-energy Hamiltonian, arising from overlap of p_z orbitals between different atomic layers in the case of chalcogenides, control the amount of tunneling from TIs to trivial insulators. Finally, we show that the same linear k_z terms in the low-energy Hamiltonian affect the material's ability to form the localised interface state, and we demonstrate that due to this effect the spin and probability density localisation in a thin film of Sb_2Te_3 is incomplete. We show that changing the parameter that controls the magnitude of the overlap of p_z orbitals affects the transport characteristics of the topologically conducting states, with incomplete topological state localisation resulting in increased backscattering.

Keywords: topological insulators, interface, position-dependent Schrödinger equation

(Some figures may appear in colour only in the online journal)

1. Introduction

Topological insulators (TIs) are a quantum state of matter identified a little over ten years ago [1]. They are commonly distinguished from trivial insulators by conducting states associated with surfaces or interfaces; the dispersion relation for these conducting states generally obeys the Dirac equation [2, 3]. Key to this classification is the fact that the existence of these states is guaranteed by the bulk properties of the topological insulator relative to the vacuum or more recognisable 'trivial' insulator on the other side of the interface [4, 5].

The electronic structure of TI junctions has been studied previously both theoretically and experimentally, often with the objective of designing spintronics-type devices or band-structure engineering towards different states of matter [6–8]. In this work we study the quantum states and dispersion relations of multiple TI junctions in a single heterostructure, by modifying an effective four-band continuum Hamiltonian previously used to capture the fundamental physics of surface states in TIs [9–16]. We apply this to a number of structures with alternating topological insulator and trivial material layers, including conductors. Because of quantum-mechanical tunneling by interface states in TIs to adjacent trivial material layers, which also results in hybridisation between interface states in proximity to each other, we have interface states that are not fully localised inside one material. This requires us

Original content from this work may be used under the terms of the Creative Commons Attribution 3.0 licence. Any further distribution of this work must maintain attribution to the author(s) and the title of the work, journal citation and DOI.

to extend the effective four-band continuum Hamiltonian to take into account the position dependence of the eight material parameters it includes.

We consider a set of substitutions in the four-band Hamiltonian that allow us to write down a system of position-dependent Schrödinger equations connecting the four bands described by the Hamiltonian. The substitutions we use are similar to those performed in the effective mass approximation for semiconductor junctions—they connect low-energy continuum Hamiltonians for one or more bands derived using $\boldsymbol{k}\cdot\boldsymbol{p}$ perturbation theory to a system of Schrödinger equations that contain position-dependent carrier masses. These substitutions are derived from making use of an envelope function approximation [17, 18]. We demonstrate how to numerically solve the system of position-dependent Schrödinger equations we obtain by making use of the finite difference approximation. Our position-dependent effective Hamiltonian applies to real systems and materials, but in this work we illustrate it by making use of a series of simulated materials defined only by the eight material parameters of the Hamiltonian, as well as making use of values of those parameters that are sometimes used in the description of the low-energy behaviour of commonly studied 3D TIs Bi_2Se_3 and Sb_2Te_3 [13–15, 19].

We aim to demonstrate the expected interface states between topological and trivial insulators, and we show that these states naturally tunnel into adjacent trivial insulator layers and hybridise with other interface states. We show the evolution of trivial bulk states into the spin-split interface states with changing topological phase. We also investigate the band mixing and inversion in both interface and bulk states, and look for possible topological features of bulk states. Additionally, we investigate the effect that the linear k_z term in the low-energy Hamiltonian, which represent p_z orbitals overlaps between different atomic layers in chalcogenide crystal structures, has on a material's ability to support localised interface states regardless of its topological phase. We investigate this effect using model parameters corresponding to real materials.

This paper is organised as follows. Section 2 describes the position-dependent effective Hamiltonian we use and discusses our numerical approach to solving our effective position-dependent Hamiltonian. In section 3 we show the electronic states and dispersion relations of multilayer heterostructures of topological and trivial materials as a function of changing material parameters, demonstrating a series of new physical effects. Section 4 contains our conclusions.

2. Model

2.1. Effective Hamiltonian

The Hamiltonian $\mathcal{H}$ used for bulk materials here is a standard 4-band model, based on that used by Liu *et al* [13] which can be written as (ignoring the k^3 terms)

$$\mathcal{H}(\boldsymbol{k}) = C(\boldsymbol{k})\mathbb{I}_4 + M(\boldsymbol{k})\Gamma_5 + Bk_z\Gamma_4 - A(k_x\Gamma_2 - k_y\Gamma_1) \tag{1}$$

where $\mathbb{I}$ is the 4×4 identity matrix,

$$\begin{aligned} C(\boldsymbol{k}) &= C_0 + C_1k_z^2 + C_2|k_{||}|^2 \\ M(\boldsymbol{k}) &= M_0 + M_1k_z^2 + M_2|k_{||}|^2 \\ k_{||} &= k_x - \mathrm{i}k_y \end{aligned} \tag{2}$$

$$\Gamma_5 = \begin{pmatrix} 1 & 0 & 0 & 0 \\ 0 & -1 & 0 & 0 \\ 0 & 0 & 1 & 0 \\ 0 & 0 & 0 & -1 \end{pmatrix}, \Gamma_4 = \begin{pmatrix} 0 & -\mathrm{i} & 0 & 0 \\ \mathrm{i} & 0 & 0 & 0 \\ 0 & 0 & 0 & -\mathrm{i} \\ 0 & 0 & \mathrm{i} & 0 \end{pmatrix},$$

$$\Gamma_2 = \begin{pmatrix} 0 & 0 & 0 & -\mathrm{i} \\ 0 & 0 & -\mathrm{i} & 0 \\ 0 & \mathrm{i} & 0 & 0 \\ \mathrm{i} & 0 & 0 & 0 \end{pmatrix}, \Gamma_1 = \begin{pmatrix} 0 & 0 & 0 & 1 \\ 0 & 0 & 1 & 0 \\ 0 & 1 & 0 & 0 \\ 1 & 0 & 0 & 0 \end{pmatrix}.$$

The constants $(C_0, C_1, C_2, M_0, M_1, M_2, A, B)$ in these definitions are material-dependent parameters; the interpretation of these parameters arises from $\boldsymbol{k}\cdot\boldsymbol{p}$ theory and their specific values for a particular material can be extracted from *ab initio* calculations or experiments. Broadly speaking, $C(\boldsymbol{k})$ represents the overall elliptical dispersion relation, M_0 is the bulk gap at the Γ point which can be positive or negative, and A and B are Rashba-type spin–orbit interaction parameters. M_1 and M_2 describe the effective masses of the quasiparticles formed by the hybridised atomic orbitals at $\boldsymbol{k}=0$, which form the basis set in which this Hamiltonian is written. This Hamiltonian describes topologically distinct phases for $M_0 > 0$ and $M_0 < 0$ [13, 15, 20] (see also appendix B), and this is the parameter we use in our simulations to continuously change our structures from TI to non-TI and back[1]. Since we are going to be looking only at k_x dispersions in this paper, we will neglect all the k_y terms in what follows. These can easily be added back in and treated the same way as k_x terms.

It is important to note that this Hamiltonian has a spin degeneracy in its energy bands. This is due to its overall time-reversal invariant nature, a key feature of $\mathbb{Z}_2$-invariant TIs [4].

We are interested in obtaining solutions to Hamiltonian (1) in systems that are bulk-like in two of three dimensions (x, y), and contain a series of interfaces in the third dimension (z) represented by infinite 2D planes in the x and y dimensions. We follow the literature (see for example [21–23]) in performing the standard substitution

$$k_z \to -\mathrm{i}\partial_z \tag{3}$$

in equation (1) to obtain the time-independent Schrödinger equation

$$\mathcal{H}(k_x, k_y)\boldsymbol{\Psi}(z) = E\boldsymbol{\Psi}(z). \tag{4}$$

In order to simulate the changing of material parameters across an interface, we will need to extend equation (1).

The approach to this problem pursued here is based on the envelope function approximation (EFA), commonly in use in traditional semiconductor physics [24, 25]. In semiconductors, the EFA leads to the effective mass approximation, which has been succesfully used to analyse semiconductor

[1] A number of different material parameter values are given in [13] that correspond to different compounds.

heterostructures by means of a single-band position-dependent Schrödinger equation [17], where the effective mass of the carriers varies with position. In line with the effective mass approximation in semiconductors, our position-dependent equation can be obtained from effective $\boldsymbol{k}\cdot\boldsymbol{p}$ Hamiltonians such as equation (1) by substituting $\boldsymbol{k}\rightarrow -\mathrm{i}\nabla$, and writing in the position dependence for our material parameters $(C_0(z), C_1(z), C_2(z), M_0(z), M_1(z), M_2(z), A(z), B(z))$. We will also need to make changes to preserve the hermiticity of the model—these are discussed in the next section.

2.2. Numerical approach

We need to rewrite equation (4) after performing the substitution in equation (3) such that it is Hermitian in regions where the material parameters are changing. This approach is similar to that historically taken in other materials e.g. wurtzite semiconductor heterostructures [26], and has also been published recently elsewhere specifically for TIs [27]. For this we use the literature standard form of the kinetic energy (see [17, 18, 24, 25]). The relevant terms that need to be rewritten are

$$\begin{aligned} -C_1\partial_z^2\mathbf{\Psi} &\rightarrow -\partial_z(C_1\partial_z\mathbf{\Psi}) \\ -M_1\Gamma_5\partial_z^2\mathbf{\Psi} &\rightarrow -\Gamma_5\partial_z(M_1\partial_z\mathbf{\Psi}) \\ -\mathrm{i}B\Gamma_4\partial_z\mathbf{\Psi} &\rightarrow -\frac{\mathrm{i}}{2}\Gamma_4\{B,\partial_z\}\mathbf{\Psi} \end{aligned} \tag{5}$$

where the curly braces indicate the usual anticommutation relation.

We now integrate equation (4) with respect to z from a point $-\epsilon$ just to the left of the interface at $z=0$ to a point ϵ just to the right of the interface. Using equations (5) and (3) we get

$$\int_{-\epsilon}^{\epsilon}\mathcal{H}_z\mathbf{\Psi}\mathrm{d}z = \int_{-\epsilon}^{\epsilon}(E\mathbf{\Psi}-\mathcal{H}_0\mathbf{\Psi})\,\mathrm{d}z \tag{6}$$

where

$$\begin{aligned} \mathcal{H}_z &= -\partial_z(C_1\partial_z) - \Gamma_5\partial_z(M_1\partial_z) - \frac{\mathrm{i}}{2}\Gamma_4\{B,\partial_z\} \\ \mathcal{H}_0 &= (C_0 + C_2k_x^2) + (M_0 + M_2k_x^2)\Gamma_5 - Ak_x\Gamma_2. \end{aligned} \tag{7}$$

In order to solve it numerically, we would like to turn equation (6) into a discretised equation. For the purposes of integration we begin by discretising the position variable z such that

$$z \rightarrow z_i = \mathrm{i}\cdot\Delta z \tag{8}$$

where i is our new lattice index variable and Δz is the lattice spacing. We introduce the wavefunction values $\mathbf{\Psi}_i$ at each point

$$\mathbf{\Psi}_i = \mathbf{\Psi}(\mathrm{i}\cdot\Delta z). \tag{9}$$

We perform the integral on the right-hand side of equation (6) by setting $\epsilon = \frac{\Delta z}{2}$ to obtain

$$\int_{-\epsilon}^{\epsilon}(E-\mathcal{H}_0)\mathbf{\Psi}\mathrm{d}z \simeq (E-\mathcal{H}_0^{(0)})\mathbf{\Psi}_0\Delta z \tag{10}$$

where the superscript (0) denotes that $\mathcal{H}_0$ uses the material parameters for site 0, which here is the interface site. Because

Table 1. Table of Hamiltonian parameters used for each figure except where indicated on the figure; non-zero values in this table are taken from [13] for Bi_2Se_3.

Parameter	Value
A/eV Å	3.33
B/eV Å	2.26
C_0/eV	0.00
C_1/eV Å^2	0.00
C_2/eV Å^2	0.00
M_0/eV	−0.28
M_1/eV Å^2	6.86
M_2/eV Å^2	44.50

we assume that the junction is symmetric, the interface site has material parameter values equal to the average of the material parameter values either side of the interface. We evaluate the integral on the left-hand side of equation (6) by parts and evaluate it at $-\frac{\Delta z}{2}$ and $\frac{\Delta z}{2}$ by interpolation using the approximations

$$\begin{aligned} \partial_z\mathbf{\Psi}(-\Delta z/2) &\simeq \frac{1}{\Delta z}(\mathbf{\Psi}_0 - \mathbf{\Psi}_{-1}) \\ \partial_z\mathbf{\Psi}(\Delta z/2) &\simeq \frac{1}{\Delta z}(\mathbf{\Psi}_1 - \mathbf{\Psi}_0) \\ \mathbf{\Psi}(-\Delta z/2) &\simeq \frac{1}{2}(\mathbf{\Psi}_0 + \mathbf{\Psi}_{-1}) \\ \mathbf{\Psi}(\Delta z/2) &\simeq \frac{1}{2}(\mathbf{\Psi}_1 + \mathbf{\Psi}_0). \end{aligned} \tag{11}$$

This finally allows us to rewrite equation (6) as

$$\mathcal{T}^{(-1)}\mathbf{\Psi}_{-1} + \mathcal{D}^{(0)}\mathbf{\Psi}_0 + \mathcal{T}^{(1)\dagger}\mathbf{\Psi}_1 = E\mathbf{\Psi}_0 \tag{12}$$

where

$$\begin{aligned} \mathcal{D}^{(i)} &= \left(C_0^{(i)} - \frac{2C_1^{(i)}}{\Delta z^2} + C_2^{(i)}k_x^2\right)\mathbb{I}_4 \\ &\quad + \left(M_0^{(i)} - \frac{2M_1^{(i)}}{\Delta z^2} + M_2^{(i)}k_x^2\right)\Gamma_5 - A^{(i)}k_x\Gamma_2 \\ \mathcal{T}^{(i)} &= \frac{C_1^{(i)}}{\Delta z^2}\mathbb{I} + \frac{M_1^{(i)}}{\Delta z^2}\Gamma_5 + \frac{\mathrm{i}B^{(i)}}{2\Delta z}\Gamma_4. \end{aligned} \tag{13}$$

The superscript (i) denotes the value of the material parameter for site i. Note that equation (12) is exactly the same as a normal second-order finite difference equation if no change in material parameters occurs across the interface—see appendix A. Equation (12) can also be extended to cover the application of a constant magnetic field in the y-direction by making use of the Peierls substitution $k_x \rightarrow k_x + \frac{e}{\hbar}B_y z$, where B_y is the field strength.

Before our results we briefly cover the numerical detail of our simulations. Other than in section 3.6, we modelled 15 nm heterostructures using 150 lattice points (1 Å lattice spacing), with interface sites at lattice points 31 and 119. The results in section 3.6 were obtained using 100 lattice points to simulate 10 nm, with no interface sites as we simulated a single slab of Sb_2Te_3. Thicknesses were chosen to minimise the amount of coupling between interface or edge states, such as that

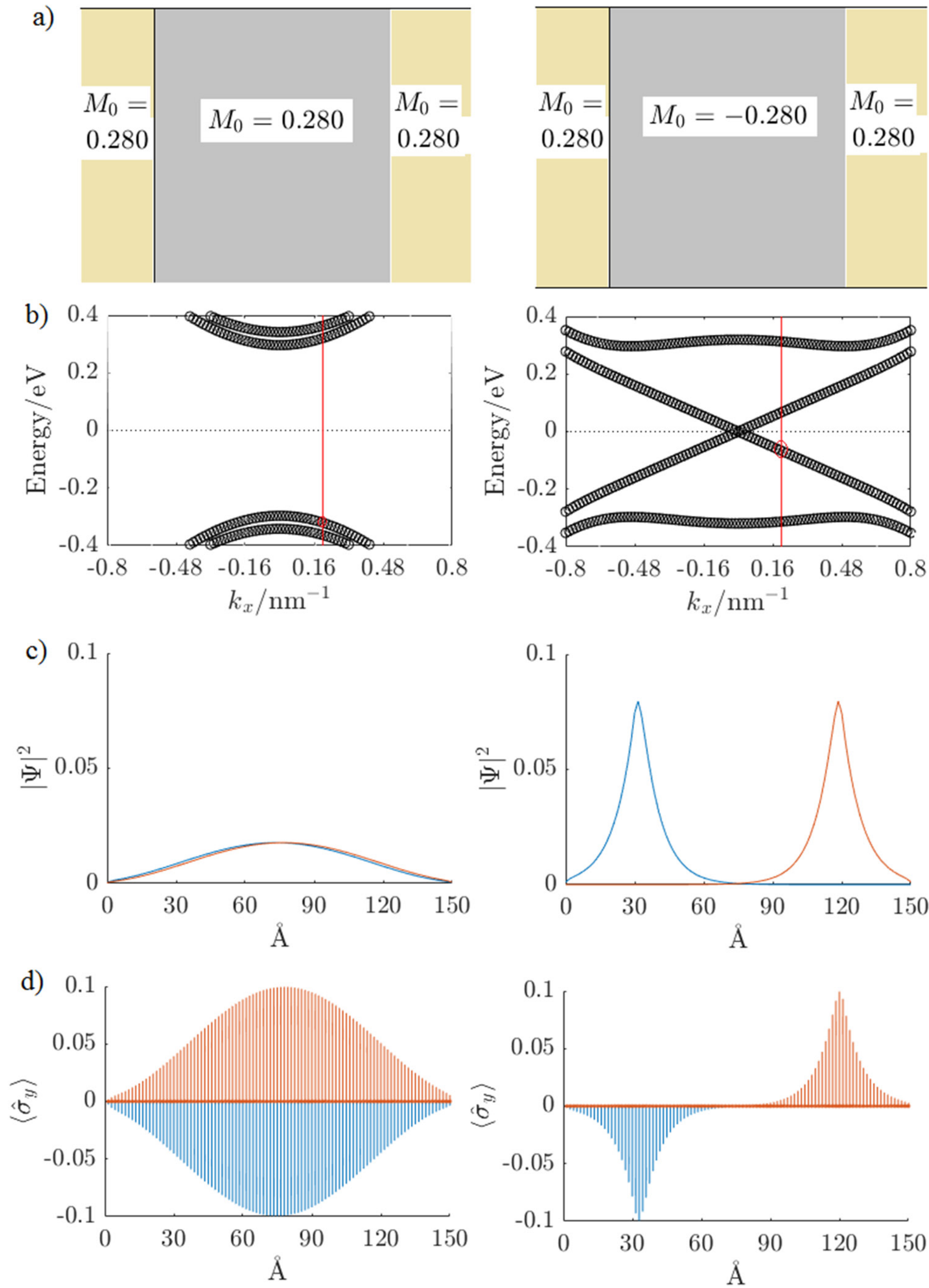

Figure 1. (a) Illustration of device, including the gap parameter used for each part. (b) Bandstructure of entire device. (c) Probability distribution of states marked in the bandstructure (b). (d) $\langle\hat{\sigma}_y\rangle$ plotted on top of the probability distribution shown in (c), indicating the spin associated with each wavefunction. Parameters given in table 1.

described in [12]—this can be seen wherever we plot bandstructures with Dirac cones, where the gap in the cone that would exist due to coupling is small enough to be invisible.

3. Results and discussion

3.1. Emergence of spin-polarised heterostructure interface states tunneling into adjacent trivial insulators

We have stated previously that the Hamiltonian (1) has distinct topological phases. These phases are controlled by the material parameter M_0, which is equal to the Γ-point energy gap between the two electronic states nearest to the Fermi level. For topologically non-trivial materials, this parameter is negative, and it indicates a crossing over of bands has occured. In Bi_2Se_3, this is the gap between the lowest bonding orbital of the hybridised Bi *p*-orbitals (labelled $|P1^+_-, \pm 1/2\rangle$), and the highest antibonding orbital of the hybridised Se *p*-orbitals (labelled $|P2^-_+, \pm 1/2\rangle$)—see [13].

In a multi-layer heterostructure, we can observe the emergence of the interface states by changing the parameter M_0 in some part of the structure. Beginning with a heterostructure of topologically-trivial materials, each with a positive gap M_0, we would expect to see a change in total probability distribution of the lowest conduction and highest valence subbands as M_0 decreases and becomes negative in part of the

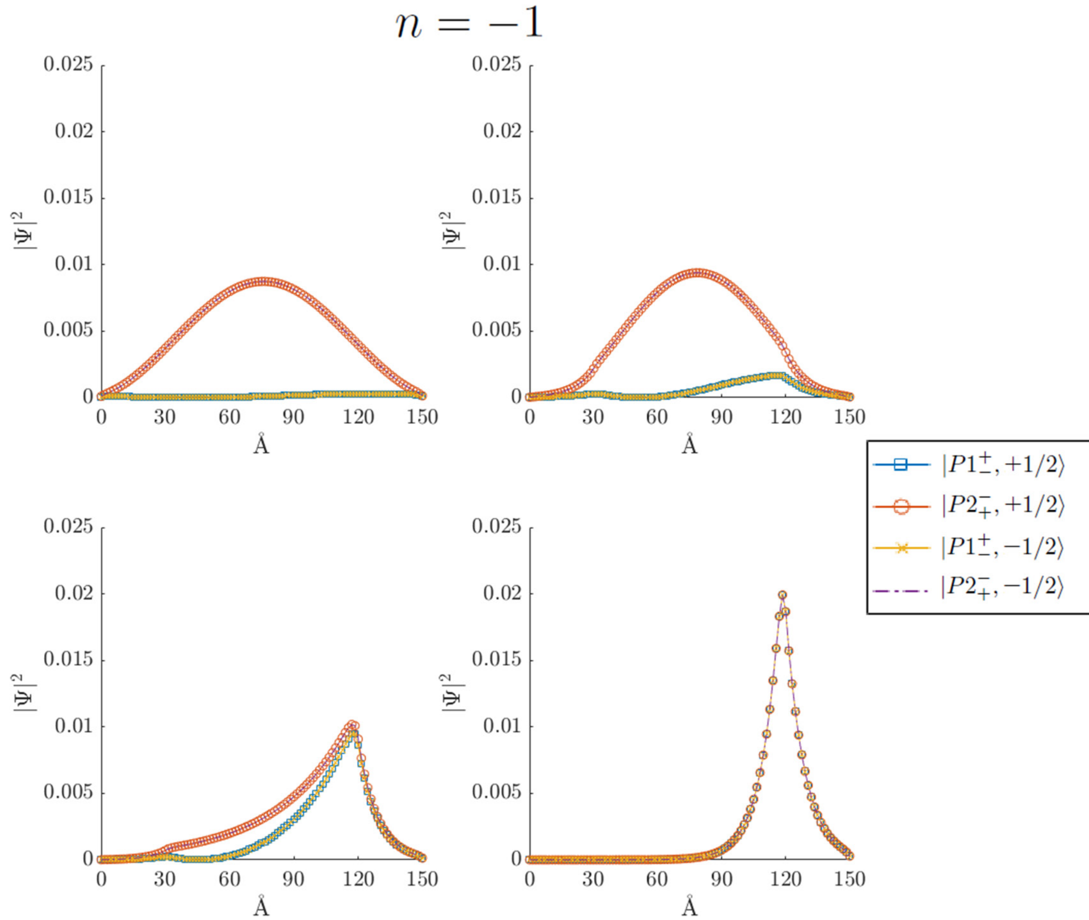

Figure 2. State from subband $n = -1$ of device as illustrated in figure 1—probability densities plotted by band component. Parameters given in table 1.

heterostructure. Figure 1 shows how they change from bulk-like states that resemble closely an electron trapped in a potential well, to states localised towards the material interfaces. Also in figure 1, we show how the subbands of the full heterostructure change as the gap M_0 closes and becomes negative. The conduction and valence bands move towards each other until they meet, and as they do they lose their parabolic character and adopt a Dirac-like linear dispersion relation about the crossing point—see figures C1 and C2 in appendix C.

Figure 1 also shows how the resulting interface states are spin-polarised—once the gap M_0 becomes negative enough, there is almost no overlap between the spin-up and spin-down interface states. This is one of the reasons for the lack of back-scattering mechanisms for electrons travelling along these interface states—in order for such an event to occur, both the crystal momentum and the spin of the electron must be reversed. In addition, it is clear that even before the change of topological phase there is some separation of the spin channels—this is due to the presence of the spin–orbit interaction, which is controlled by the parameters A and B in the Hamiltonian (1).

3.2. Evidence of complete mixing of conduction and valence orbitals in the topological interface state

The states presented in figure 1 are shown as probability distributions in space over all four basis states of the Hamiltonian. However, we would not necessarily expect the electronic occupation of each basis state of the Hamiltonian to be equal in each case.

One important point about the topological interface states in a finite-size device such as the ones studied in this work, is that they are an example of one of many subbands that are formed in a finite device. These subbands are distinct from the bulk bands that are described at the start of section 3.1, labelled $|P1^+_-, \pm 1/2\rangle$ and $|P2^-_+, \pm 1/2\rangle$. However, this section, and section 3.4, are concerned with the four components of a particular subband; those four components can be traced back to the bulk states $|P1^+_-, \pm 1/2\rangle$ and $|P2^-_+, \pm 1/2\rangle$ by examining the form of the numerical Hamiltonian (12).

In figure 2, we plot the occupation of each basis orbital as a function of position in the heterostructure, for one of the two highest valence orbitals. We find that, for the topologically trivial cases where the gap M_0 is positive throughout the structure, the electrons in the highest valence band occupy primarily the $|P2^-_+, \pm 1/2\rangle$ states. We find this to be an expected result—before the band inversion caused by the spin–orbit interaction, the $P2$ orbitals represent the highest energy orbital that is still below the Fermi level [13]. As the gap M_0 is made negative for the part of the heterostructure indicated on figure 2, we see for the highest valence orbital that the $|P1^+_-, \pm 1/2\rangle$ states begin to match the $|P2^-_+, \pm 1/2\rangle$ states in terms of occupation. It is clear that the surface states are formed of a mixture of the two sets

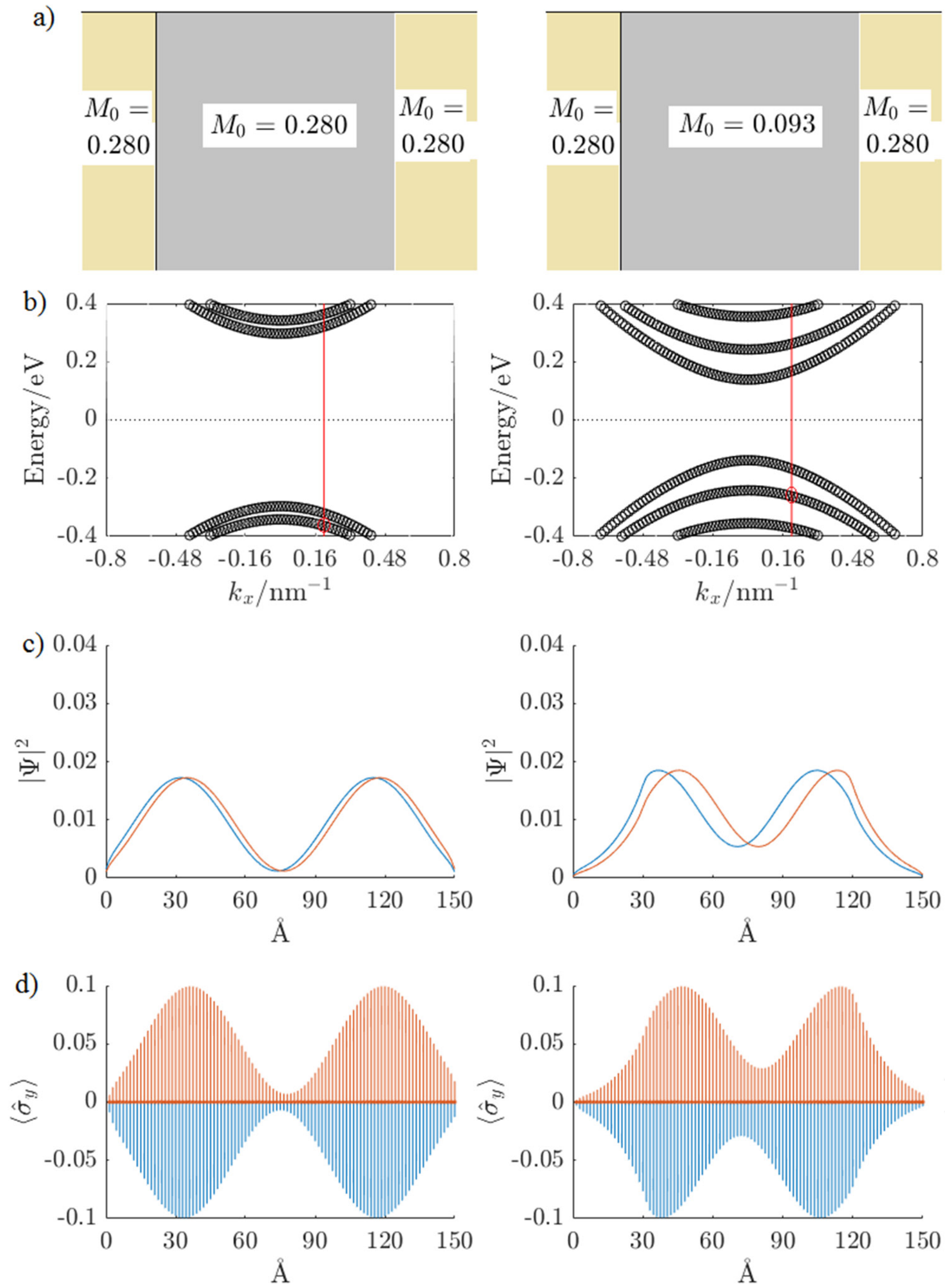

Figure 3. (a) Illustration of device, including the gap parameter used for each part. (b) Bandstructure of entire device. (c) Probability distribution of states marked in the bandstructure (b). (d) $\langle\hat{\sigma}_y\rangle$ plotted on top of the probability distribution shown in (c), indicating the spin associated with each wavefunction. Parameters given in table 1.

of states, as the spin orbit interaction in the crystal brings them together and inverts them, changing the topological phase of the material.

3.3. Evidence of topological features of heterostructure bulk states

We turn our attention now to the bulk states just above and just below the bands that form the interface states. We define here bulk states as those states which are associated with bands that remain parabolic or quartic throughout our parameter sweep; these are states with probability distributions which are spread further away from the material interface. These states also experience some changes in probability distribution and orbital composition as the relevant part of the heterostructure changes topological phase.

Figures 3 and 4 plot the evolution of the bulk valence bands closest to the interface states. We can see that at the highlighted point $k_x = 0.2\mathrm{nm}^{-1}$ on the bandstructure, the probability distribution of the resulting state shifts with the change in topological phase from a bimodal distribution to one with a single maximum. Both the initial and the final states shown are reminiscent of the states of an electron in a potential well, but we have moved from two nodes to one node. The quantized electron in a potential well has states such that each extra node—each additional maximum in the probability

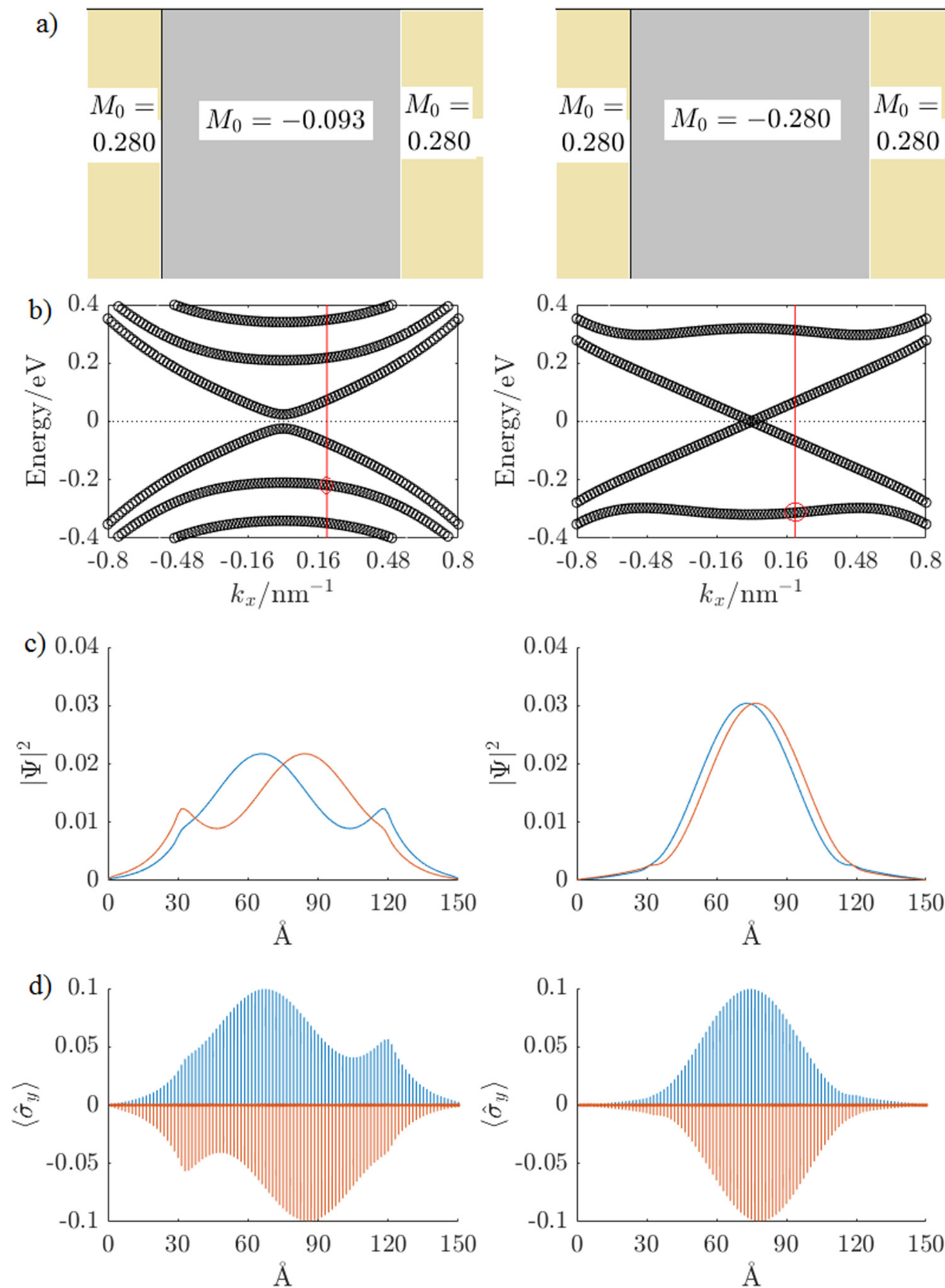

Figure 4. (a) Illustration of device, including the gap parameter used for each part. (b) Bandstructure of entire device. (c) Probability distribution of states marked in the bandstructure (b). (d) $\langle\hat{\sigma}_y\rangle$ plotted on top of the probability distribution shown in (c), indicating the spin associated with each wavefunction. Parameters given in table 1.

distribution—represents an additional unit of energy. We can see that where we have lost the lowest energy, zero-node distribution state in figure 1 as it forms into an interface state, we have gained a new zero-node distribution state in figures 3 and 4. However, the shapes of these distributions are not identical. We can see from figures 3 and 4 compared to figure 1 that the zero-node bulk state has an additional kink towards the edge of the heterostructure, near to the interface (highlighted in the figure). It appears likely that this bulk state is affected by the topological phase transition in this area.

It is also clear from figures 3 and 4 that there is some spin polarisation across the heterostructure in these bulk states. Again, this is due to the spin orbit interaction in these materials, and the non-zero crystal momentum of these states. We would expect to see similar effects in all of the states created by our simulations.

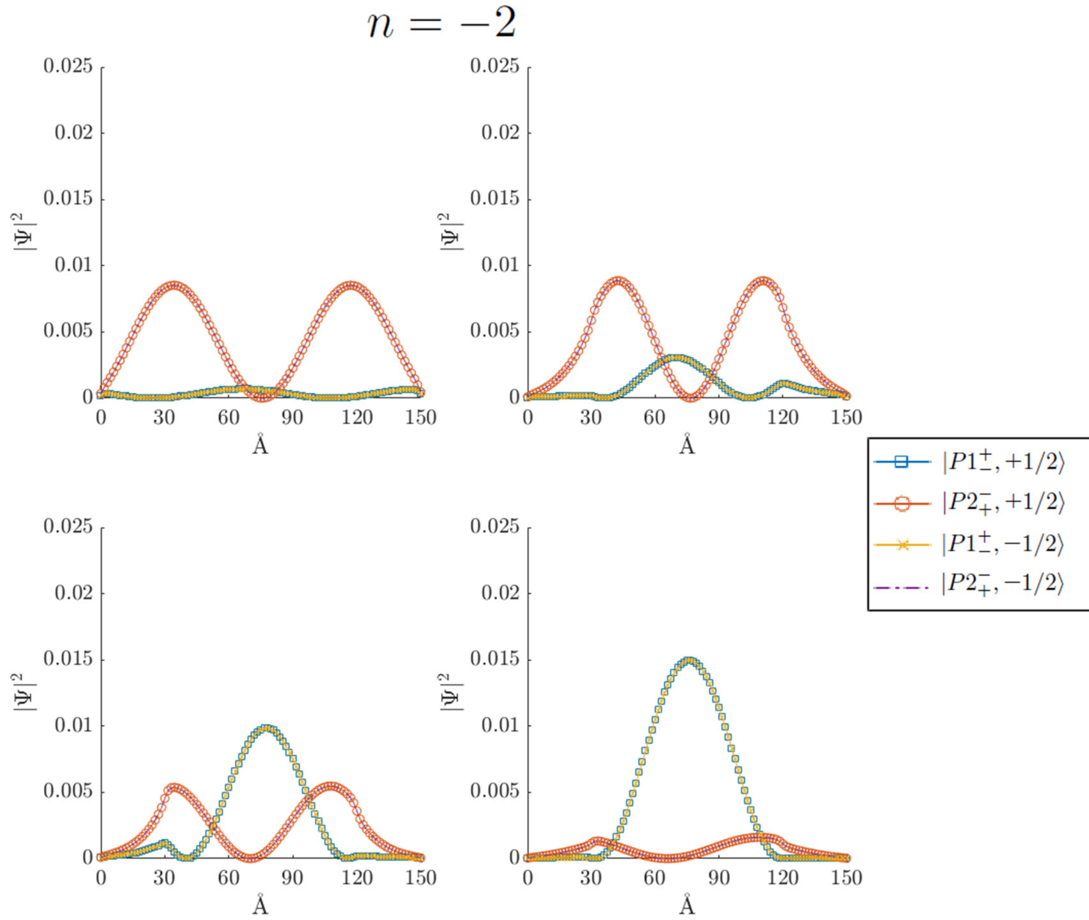

Figure 5. State from subband $n = -2$ of device as illustrated in figure 1—probability densities plotted by band component. Parameters given in table 1.

3.4. Evidence of complete and incomplete band inversion in heterostructure bulk states of different energies relative to the gap

We can also demonstrate bulk band inversion within the heterostructure by examining the composition of the bulk state in terms of the Hamiltonian basis states—the $|P1^+_-, \pm 1/2\rangle$ bonding states and the $|P2^-_+, \pm 1/2\rangle$ antibonding states, as discussed previously. Figure 5 shows the probability distribution of one of the highest energy valence bulk states, plotting the magnitude of each of the four components. We can see that much like in the case of the interface state that arises from the valence band, the state starts of dominated by the $|P2^-_+, \pm 1/2\rangle$ antibonding states. As the gap M_0 of the structure is changed, we find that occupation of the $|P1^+_-, \pm 1/2\rangle$ bonding states increases, and by the time the structure has reached a negative enough gap, the $|P1^+_-, \pm 1/2\rangle$ bonding states become the dominant component of this valence bulk state. While this image is not included here, we find the same kind of inversion from $|P1^+_-, \pm 1/2\rangle$ bonding states to $|P2^-_+, \pm 1/2\rangle$ antibonding states takes place in the lowest parts of the conduction band.

However, further away from the gap the inversion is less complete, and in fact no inversion occurs in the trivial insulator parts of the heterostructure. We illustrate this phenomenon in figure 6. Inside the topological insulator, the bulk state contains a mixture of the $|P1^+_-, \pm 1/2\rangle$ bonding and $|P2^-_+, \pm 1/2\rangle$ antibonding states, while inside the trivial insulators the bulk state contains only $|P2^-_+, \pm 1/2\rangle$ antibonding states. This fits with the expected ordering of the bonding and antibonding states in trivial and TIs. It is also to be expected that the further away a band is from the gap, the less affected it will be by the topological crossover of the bonding and antibonding states.

3.5. Demonstrating control of interface state tunneling into adjacent trivial insulator by p_z-orbital interactions

In the devices studied so far, we have been focusing on the effect of changing the primary topological parameter, the band gap M_0. We have been studying the topological phase transition controlled by this parameter. However, there are more subtle effects taking place at the TI-trivial insulator boundary that are controlled by other parameters in the Hamiltonian. In this section and the next we consider the parameter B, which is found from $\boldsymbol{k} \cdot \boldsymbol{p}$ theory to be [13]

$$B = \frac{\hbar}{m}\langle P1^+_-, \frac{1}{2}|p_z|P2^-_+, \frac{1}{2}\rangle$$
$$= -\frac{\hbar}{m}\langle P1^+_-, -\frac{1}{2}|p_z|P2^-_+, -\frac{1}{2}\rangle. \qquad (14)$$

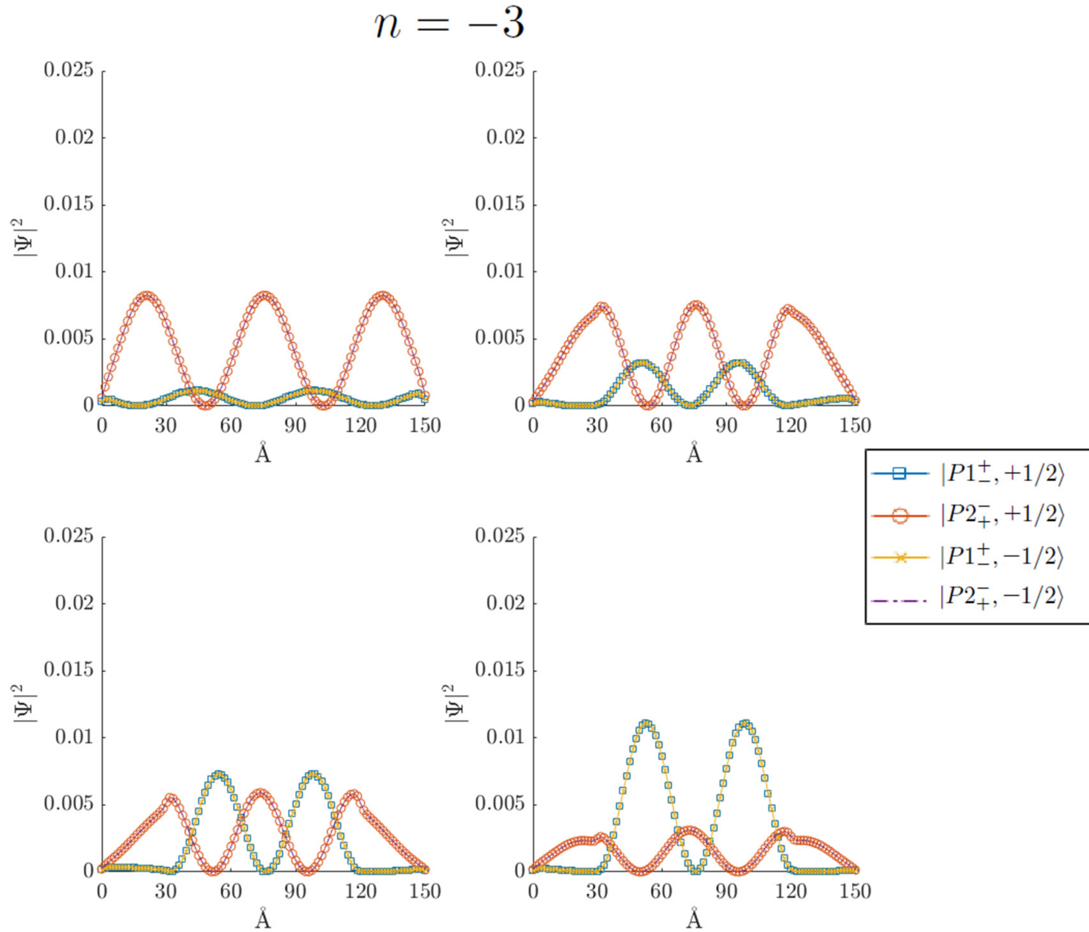

Figure 6. State from subband $n = -3$ of device as illustrated in figure 1—probability densities plotted by band component. Parameters given in table 1.

In the absence of the spin–orbit interaction, this parameter is zero [25]. From equation (14) and by comparison with Hamiltonian (1), we can see that the B parameter is responsible for mixing $|P1^+_-, \pm 1/2\rangle$ bonding and $|P2^-_+, \pm 1/2\rangle$ antibonding states. Having seen in previous sections that the TI-trivial insulator interface state is a mixed state of the bonding and antibonding states, we would expect to see some impact on the interface state from variations of the B parameter.

In figure 7 we plot the total probability density of one of the interface states across a trivial-TI-trivial heterostructure for four different values of B. We find in this figure that the B parameter controls the depth of tunneling of the interface state into the trivial insulator, separately from the bandgap of the trivial insulator. Decreasing the B parameter in the trivial insulator relative to the topological insulator decreases the tunneling depth of the interface state into the trivial insulator. Similarly, increasing the B parameter in the trivial insulator will increase the amount of tunneling.

On an atomic level, the overlap in equation (14) is dominated by the interaction of the p_z orbitals of Bi and Se respectively (in the case of Bi_2Se_3, or their equivalent atoms in other chalcogenides and alloys of chalcogenides). These will be affected by the atomic lattice spacing and the relevant outmost shells of the atoms in question ($6p$ for Bi, $5p$ for Sb and Te, $4p$ for Se). We would expect, for example, that the overlap with the $5p$ orbitals of Sb atoms would be smaller than the $6p$ orbitals of Bi, which have probability density spread much further away from the nucleus. We explore this prediction in the next section.

3.6. Evidence of incomplete localisation of surface states of Sb_2Te_3 due to reduced p_z-orbital interactions

So far we have used models with particle-hole symmetry to examine effects inside TI-trivial insulator heterostructures. Here, we employ parameters for a known material, Sb_2Te_3, to identify new features in its surface states. We established in the previous section that the atomic p_z orbital overlap between the different layers of the chalcogenide affects the formation of the interface state. This overlap is controlled in Hamiltonian (1) by the parameter B. [13] gives material parameter values for each of three materials, which we reproduce in table 2.

By comparing the entries for M_0 and B for the two materials, we can see that the spin–orbit coupling that inverts the bonding and antibonding bands is weaker in Sb_2Te_3 than in Bi_2Se_3. With the lattice vectors of Sb_2Te_3 being similar to those of Bi_2Se_3 [19, 28], one possible suggestion for the weaker p_z overlap is that the much closer distribution of the

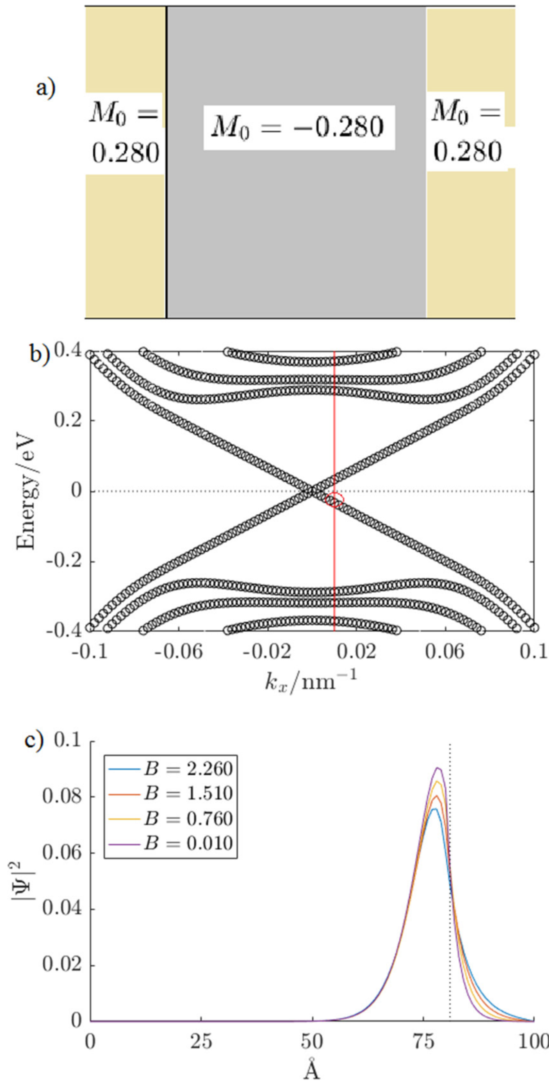

Figure 7. (a) Device illustration. (b) Bandstructure of device illustrated in (a). (c) Probability density of state indicated in (b), changing with the Hamiltonian parameter *B*. Parameters given in table 1.

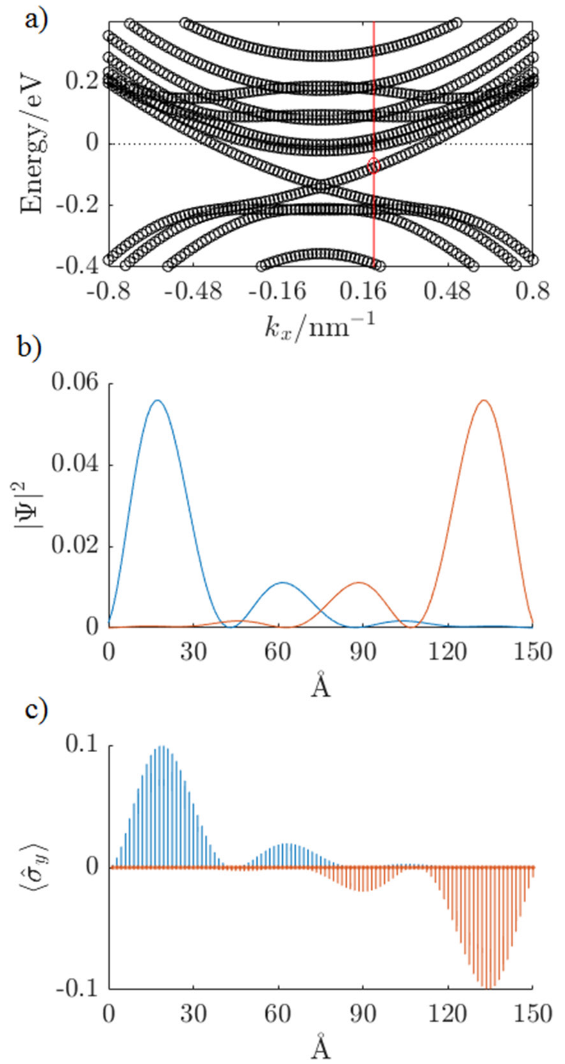

Figure 8. (a) Bandstructure of 10nm slab of Sb_2Te_3 as modelled by parameters in table 2 taken from [13]. (b) Probability density of state indicated in (a). (c) $\langle\hat{\sigma}_y\rangle$ plotted on top of the probability distribution shown in (b), indicating the spin associated with each wavefunction.

Table 2. Table of Hamiltonian parameters used for these results taken from Liu *et al* [13].

Parameter	Bi_2Se_3	Sb_2Te_3
A/eV Å	3.33	3.40
B/eV Å	2.26	0.84
C_0/eV	−0.0083	0.001
C_1/eV Å^2	5.74	−12.39
C_2/eV Å^2	30.4	−10.78
M_0/eV	−0.28	−0.22
M_1/eV Å^2	6.86	19.64
M_2/eV Å^2	44.50	48.51

Sb $5p_z$ orbital compared to the Bi $6p_z$ orbital, as well as the reduced spin orbit interaction due to decreased mass, is not offset by the increase in ionic mass and orbital diffusion by moving from the Se ion and $4p_z$ orbital to the Te ion and $5p_z$ orbital.

Figure 8 shows the low-energy bandstructure of Sb_2Te_3 as reproduced by Hamiltonian (1) using the parameters from table 2, and the probability distribution and spin expectation value of the surface state that is indicated on the bandstructure. We can see that the surface state is no longer confined around the edge, but has nodes further into the core of the TI slab. In fact, there are spin up and spin down nodes overlapping in the centre of the structure, which creates the possibility for backscattering in the edge states. As discussed above, we believe this is the result of the weaker overlap of Sb and Te $5p_z$ orbitals relative to the same overlaps in Bi_2Se_3. This is an important result, because it suggests that the effectiveness of topologically protected surface conduction can be undermined by atomic-level features separate to the topological phase of the material. We investigate this further in the next section.

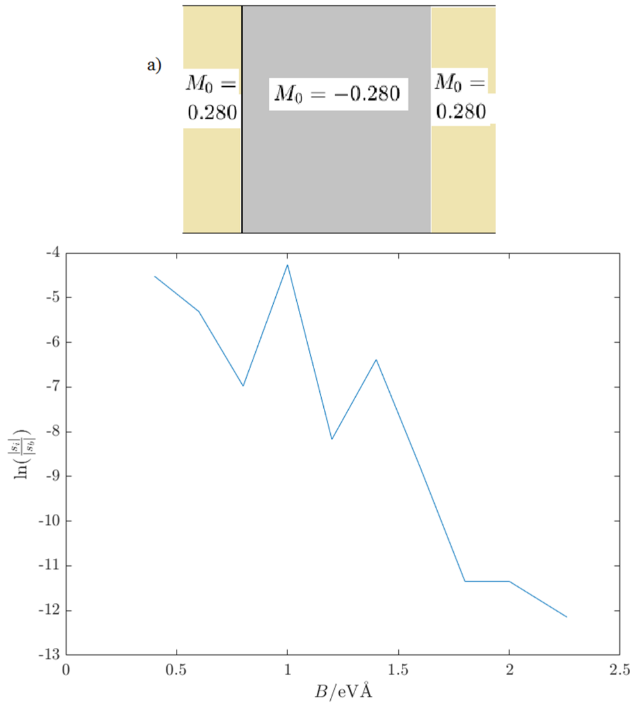

Figure 9. (a) Device illustration. (b) Logarithm of backscattering matrix element of surface state as a fraction of backscattering matrix element of bulk state, versus the value of B. Parameters given in table 1.

3.7. Backscattering measurements

We make use of our simulated wavefunctions from solving equation (1) to calculate the effect on the backscattering in interface states due to the change in the B parameter, which represents the dipole matrix element between the p_z orbitals of the different atomic layers of the chalcogenide. We consider two modes of longitudinal transport in the $x - y$ plane, through a cross-section of a device such as the one illustrated in figure 7 which is finite in the z-dimension. For a Fermi level close to the Dirac point, conduction takes place through two sets of spin-locked interface states (see figures 1 and 8). Each spin-locked set has a forward and backward moving mode associated with it ($+k_x$ or $-k_x$). Scattering between the different spin states is not possible [1], so we focus on two modes—forward and backward—with the same spin.

To measure the backscattering, we follow [29] in making use of the Green's function in the form

$$G^R(y, z; y', z') = -\frac{\mathrm{i}}{\hbar v}\boldsymbol{\Psi}(z) \cdot \boldsymbol{\Psi}(z') \tag{15}$$

where z and z' are defined at the terminals $y = 0$ and $y' = 0$, v is the electron velocity, and $\boldsymbol{\Psi}(z)$ is the subband which solves equation (4). From the Green's function we make use of the Fisher-Lee relation

$$s_{qp} = -\delta_{qp} + \mathrm{i}\hbar\sqrt{v_q v_p}G^R_{qp}, \tag{16}$$

where q and p label device terminals, to find the backscattering matrix element $q = p$ (in terms of equation (15), $y = y'$).

Figure 9(b) shows the magnitude of the backscattering matrix element s_{pp} for the interface state (labelled $|s_i|$) plotted as a fraction of the magnitude of the backscattering matrix element for the bulk state (labelled $|s_b|$), against the value of the parameter B, for the device shown in figure 9(a), using material parameters in table 1. We can see clear evidence of an increase in backscattering as the value of B decreases, though this is clearly not linear.

4. Conclusion and outlook

In this article we have investigated the bulk and interface quantum states of electrons in multi-layer heterostructures of topological and trivial materials. We made use of an effective four-band continuum Hamiltonian by treating the eight material parameters of the Hamiltonian as position-dependent.

We have shown that, as expected, spin-polarised interface states form in the heterostructure, and tunnel a finite distance into trivial insulators. We have presented evidence of complete mixing of conduction and valence bands in interface states. We have shown that bulk states in TI heterostructures exhibit features not present in trivial insulator heterostructures, and that there exists a varying degree of conduction and valence band mixing in bulk states according to energy. We have shown that the p_z orbital overlap between neighbouring atomic layers in a chalcogenide can affect the tunneling of the interface state into a neighbouring trivial insulator. Finally, we present evidence that the surface states of Sb_2Te_3 may not be completely localised at the edges, due to a lower amount of p_z orbital overlap in that crystal relative to the more closely studied TI of the same family, Bi_2Se_3. We showed that this could potentially impact the transport through the surface states due to creating the possibility of backscattering.

Our system relied on realistic physical parameters drawn from fitting of the Hamiltonian (1) to *ab initio* calculations in Bi_2Se_3 and Sb_3Te_3 [13]. Other materials could be fitted using the eight parameters of the model, and our analysis could be compared to other studies of those materials. In addition, [13] presents extensions of Hamiltonian (1) that take into account the hexagonal warping of the Dirac cone highly prominent in materials such as Bi_2Te_3 [19], which can also be included in our analysis by extending the finite difference approximation to higher order derivatives. It would be very interesting to see *ab initio* calculations that model a sequence of alloys with relatively similar material properties but changing B parameter (p_z orbital dipole matrix element) in order to compare to our results—this is something we are interested in pursuing in a further publication. The approach we have outlined here is powerful enough to apply to multiple interfaces across various different materials as required, and thus should be of interest to anyone in the field looking for a first approach to modelling a heterostructure of mixed topological phase.

Acknowledgments

AN would like to thank the EPSRC for funding his work. KZ's work was made possible by the CSC Cambridge Scholarship sponsored by China Scholarship Council and Cambridge Trust. The authors would like to thank Professor Chris Ford, Dr Thierry Ferrus, Angadjit Singh and Ankita Anirban for useful discussions.

Appendix A. Finite difference approximation

The finite difference approximations made throughout this paper consist of the following substitutions:

$$\partial_j \Phi(\boldsymbol{r}) \rightarrow \frac{1}{2h}(\Phi(\boldsymbol{r}+h\boldsymbol{j}) - \Phi(\boldsymbol{r}-h\boldsymbol{j})) \tag{A.1}$$

$$\partial_j^2 \Phi(\boldsymbol{r}) \rightarrow \frac{1}{h^2}(\Phi(\boldsymbol{r}+h\boldsymbol{j}) - 2\Phi(\boldsymbol{r}) + \Phi(\boldsymbol{r}-h\boldsymbol{j})) \tag{A.2}$$

where $j = x, y, z$ labels the direction of differentiation, the vector $\boldsymbol{j}$ is the unit vector in that direction, and h is the discretisation length. These are standard substitutions—for more detail any numerics textbook can be consulted (see for example [30]).

Appendix B. Calculating the Berry flux through the model

The Berry flux through the Brillouin zone of the system is a commonly encountered topological quantum number in the study of TIs [3]. We can analyse the Hamiltonian (1) to get a sense for when this number is not zero (and hence where the model enters a different topological phase of matter). The eigenstates of the bulk Hamiltonian are found to be

$$\begin{aligned}
\boldsymbol{\Psi}_1^T(\boldsymbol{k}) &= \frac{1}{\sqrt{N(\boldsymbol{k})}}(-\mathrm{i}Bk_z, \sqrt{P(\boldsymbol{k})} - M(\boldsymbol{k}), \mathrm{i}Ak_{\|}, 0) \\
\boldsymbol{\Psi}_2^T(\boldsymbol{k}) &= \frac{1}{\sqrt{N'(\boldsymbol{k})}}(\sqrt{P(\boldsymbol{k})} + M(\boldsymbol{k}), -\mathrm{i}Bk_z, 0, \mathrm{i}Ak_{\|}) \\
\boldsymbol{\Psi}_3^T(\boldsymbol{k}) &= \frac{1}{\sqrt{N'(\boldsymbol{k})}}(-\mathrm{i}Bk_z, -\sqrt{P(\boldsymbol{k})} - M(\boldsymbol{k}), \mathrm{i}Ak_{\|}, 0) \\
\boldsymbol{\Psi}_4^T(\boldsymbol{k}) &= \frac{1}{\sqrt{N(\boldsymbol{k})}}(-\sqrt{P(\boldsymbol{k})} + M(\boldsymbol{k}), -\mathrm{i}Bk_z, 0, \mathrm{i}Ak_{\|})
\end{aligned} \tag{B.1}$$

where

$$\begin{aligned}
P(\boldsymbol{k}) &= A^2k_{\|}^2 + B^2k_z^2 + (M(\boldsymbol{k}))^2 \\
N(\boldsymbol{k}) &= 2M(\boldsymbol{k})(M(\boldsymbol{k}) - \sqrt{P(\boldsymbol{k})}) \\
N'(\boldsymbol{k}) &= 2M(\boldsymbol{k})(M(\boldsymbol{k}) + \sqrt{P(\boldsymbol{k})})
\end{aligned} \tag{B.2}$$

and $M(\boldsymbol{k})$ is defined in equation (2). Note that $\boldsymbol{\Psi}_1$ and $\boldsymbol{\Psi}_4$ vanish completely at the time-reversal invariant momentum (TRIM) point $\boldsymbol{k} = 0$. The Berry connection $\boldsymbol{A}(\boldsymbol{k})$ is defined as

$$\boldsymbol{A}(\boldsymbol{k}) = \mathrm{i}\langle \boldsymbol{\Psi}(\boldsymbol{k}) | \nabla_k \boldsymbol{\Psi}(\boldsymbol{k}) \rangle \tag{B.3}$$

where $|\nabla_k \boldsymbol{\Psi}(\boldsymbol{k})\rangle$ is defined by

$$\langle \boldsymbol{\Phi} | \nabla_k \boldsymbol{\Psi}(\boldsymbol{k}) \rangle = \nabla_k \langle \boldsymbol{\Phi} | \boldsymbol{\Psi}(\boldsymbol{k}) \rangle. \tag{B.4}$$

By inserting the projection operator $|\boldsymbol{k}\rangle\langle\boldsymbol{k}|$ into equation (B.3) and integrating by parts we obtain

$$\boldsymbol{A}(\boldsymbol{k}) = \frac{\mathrm{i}}{2}\nabla_k(\boldsymbol{\Psi}^T(\boldsymbol{k})\boldsymbol{\Psi}(\boldsymbol{k})). \tag{B.5}$$

It is not necessary to expand this equation to completion to evaluate where the Berry flux through the Brillouin zone will be zero. Consider the definition of the Berry flux, which here is a scalar value obtained from a 2D curl operator:

$$B(\boldsymbol{k}) = \nabla_{2\mathrm{D}} \times \boldsymbol{A}(\boldsymbol{k}). \tag{B.6}$$

This is zero where $\boldsymbol{A}$ is finite by the well-known vector calculus theorem $\nabla \times \nabla g = 0$. However, we can see by examining the forms of the normalisation constants $N(\boldsymbol{k})$ and $N'(\boldsymbol{k})$ in equation (B.2) that it is possible for $\boldsymbol{A}$ to stop being finite (and thus the Berry flux $B(\boldsymbol{k})$ to become non-zero) where these constants become zero, which is only possible for both constants simultaneously if M_0 and $M_{1,2}$ have different signs. As $M_{1,2}$ have physical interpretations as quasi-particle masses and so are generally thought of as positive [13], this allows us to recover the topological insulator condition for the Hamiltonian $M_0 < 0$. A vanishing normalisation constant is commonly encountered in the analysis of topologically nontrivial mappings from the Hilbert space of the Hamiltonian to the torus of the Brillouin zone. This occurs because there is no single choice of global coordinates in $\boldsymbol{k}$-space that can consistently define the eigenvectors at each point in the Brillouin zone.

Appendix C. Detailed figures of creation of interface states

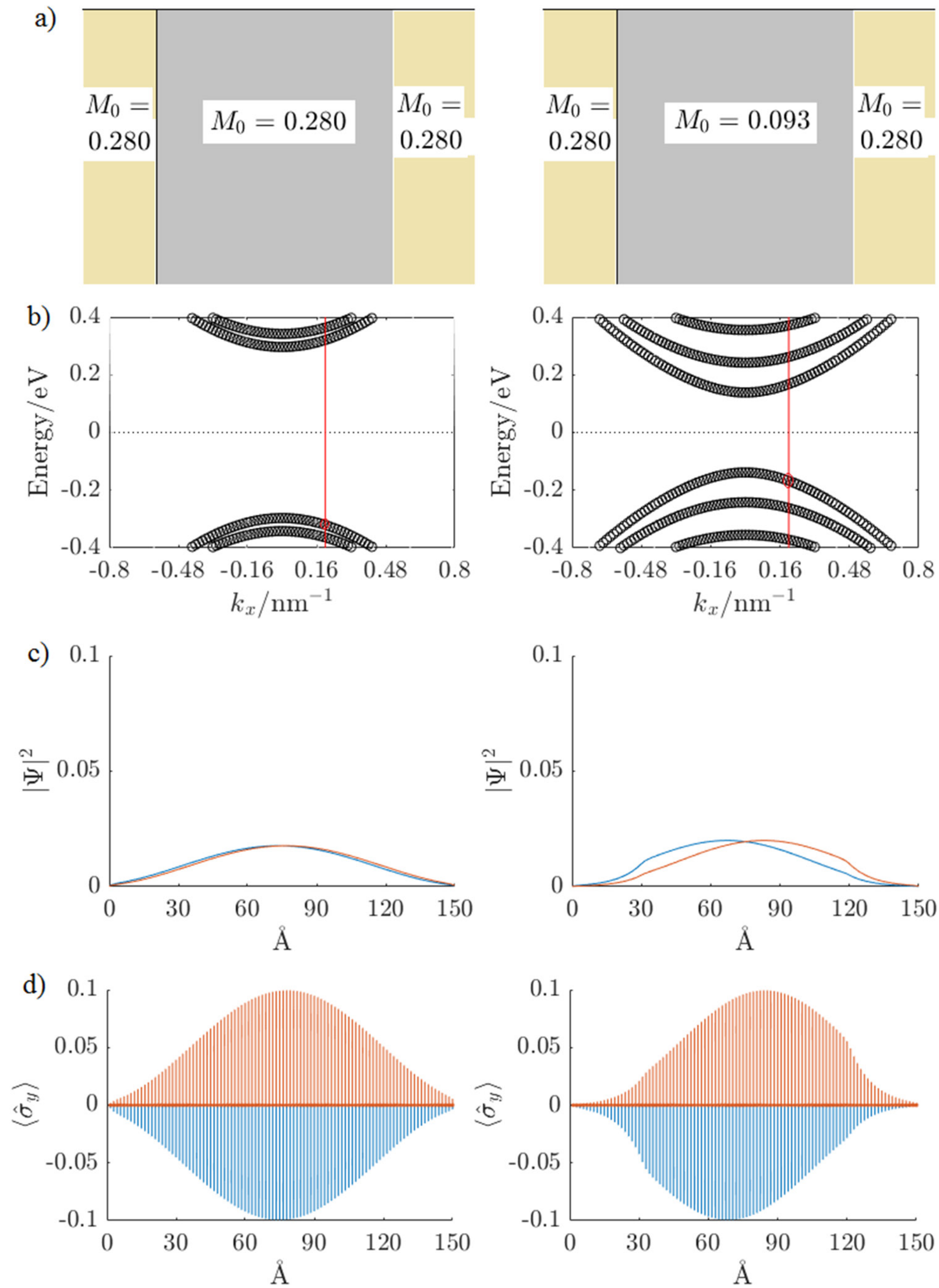

Figure C1. (a) Illustration of device, including the gap parameter used for each part. (b) Bandstructure of entire device. (c) Probability distribution of states marked in the bandstructure (b). (d) $\langle\hat{\sigma}_y\rangle$ plotted on top of the probability distribution shown in (c), indicating the spin associated with each wavefunction.

Figure C2. (a) Illustration of device, including the gap parameter used for each part. (b) Bandstructure of entire device. (c) Probability distribution of states marked in the bandstructure (b). (d) $\langle\hat{\sigma}_y\rangle$ plotted on top of the probability distribution shown in (c), indicating the spin associated with each wavefunction.

ORCID iDs

Aleksandar Nikolic https://orcid.org/0000-0001-5784-0316

References

[1] Kane C L and Mele E J 2005 Quantum spin Hall effect in graphene *Phys. Rev. Lett.* **95** 226801
[2] Hasan M Z and Kane C L 2010 Colloquium: topological insulators *Rev. Mod. Phys.* **82** 3045
[3] Ando Y 2013 Topological insulator materials *J. Phys. Soc. Japan* **82** 102001
[4] Kane C L and Mele E J 2005 Z_2 topological order and the quantum spin Hall effect *Phys. Rev. Lett.* **95** 146802
[5] Fu L, Kane C L and Mele E J 2007 Topological insulators in three dimensions *Phys. Rev. Lett.* **98** 106803
[6] Fan Y *et al* 2014 Magnetization switching through giant spin–orbit torque in a magnetically doped topological insulator heterostructure *Nat. Mater.* **13** 699
[7] Kandala A, Richardella A, Rench D, Zhang D, Flanagan T and Samarth N 2013 Growth and characterization of hybrid insulating ferromagnet-topological insulator heterostructure devices *Appl. Phys. Lett.* **103** 202409
[8] Burkov A A and Balents L 2011 Weyl semimetal in a topological insulator multilayer *Phys. Rev. Lett.* **107** 127205

[9] Bernevig B A, Hughes T L and Zhang S-C 2006 Quantum spin Hall effect and topological phase transition in HgTe quantum wells *Science* **314** 1757–61
[10] König M, Wiedmann S, Brüne C, Roth A, Buhmann H, Molenkamp L W, Qi X-L and Zhang S-C 2007 Quantum spin Hall insulator state in HgTe quantum wells *Science* **318** 766–70
[11] König M, Buhmann H, Molenkamp L W, Hughes T, Liu C-X, Qi X-L and Zhang S-C 2008 The quantum spin Hall effect: theory and experiment *J. Phys. Soc. Japan* **77** 031007
[12] Zhou B, Lu H-Z, Chu R-L, Shen S-Q and Niu Q 2008 Finite size effects on helical edge states in a quantum spin-Hall system *Phys. Rev. Lett.* **101** 246807
[13] Liu C-X, Qi X-L, Zhang H J, Dai X, Fang Z and Zhang S-C 2010 Model Hamiltonian for topological insulators *Phys. Rev.* B **82** 045122
[14] Zhang H, Liu C-X, Qi X-L, Dai X, Fang Z and Zhang S-C 2009 Topological insulators in Bi_2Se_3, Bi_2Te_3 and Sb_2Te_3 with a single Dirac cone on the surface *Nat. Phys.* **5** 438
[15] Shan W-Y, Lu H-Z and Shen S-Q 2010 Effective continuous model for surface states and thin films of three-dimensional topological insulators *New J. Phys.* **12** 043048
[16] Linder J, Yokoyama T and Sudbø A 2009 Anomalous finite size effects on surface states in the topological insulator Bi_2Se_3 *Phys. Rev.* B **80** 205401
[17] Bastard G 1981 Superlattice band structure in the envelope-function approximation *Phys. Rev.* B **24** 5693
[18] Jha P K, Eleuch H and Rostovtsev Y V 2011 Analytical solution to position dependent mass Schrödinger equation *J. Mod. Opt.* **58** 652–6
[19] Zhang W, Yu R, Zhang H-J, Dai X and Fang Z 2010 First-principles studies of the three-dimensional strong topological insulators Bi_2Te_3, Bi_2Se_3 and Sb_2Te_3 *New J. Phys.* **12** 065013
[20] Lu H-Z, Shan W-Y, Yao W, Niu Q and Shen S-Q 2010 Massive Dirac fermions and spin physics in an ultrathin film of topological insulator *Phys. Rev.* B **81** 115407
[21] Brey L and Fertig H A 2014 Electronic states of wires and slabs of topological insulators: quantum Hall effects and edge transport *Phys. Rev.* B **89** 085305
[22] Zhang L, Chang K, Xie X, Buhmann H and Molenkamp L 2010 Quantum tunneling through planar p–n junctions in HgTe quantum wells *New J. Phys.* **12** 083058
[23] Deb O, Soori A and Sen D 2014 Edge states of a three-dimensional topological insulator *J. Phys.: Condens. Matter* **26** 315009
[24] Ridley B K 2009 *Electrons and Phonons in Semiconductor Multilayers* vol 5 (Cambridge: Cambridge University Press)
[25] Winkler R 2003 Spin–orbit coupling effects in two-dimensional electron and hole systems *Springer Tracts Mod. Phys.* **191** 153–6
[26] Chuang S and Chang C 1997 A band-structure model of strained quantum-well wurtzite semiconductors *Semicond. Sci. Technol.* **12** 252
[27] Sengupta P, Ryu H, Lee S, Tan Y and Klimeck G 2016 Numerical guidelines for setting up a k.p simulator with applications to quantum dot heterostructures and topological insulators *J. Comput. Electron.* **15** 115–28
[28] Sosso G, Caravati S and Bernasconi M 2009 Vibrational properties of crystalline Sb_2Te_3 from first principles *J. Phys.: Condens. Matter* **21** 095410
[29] Datta S 1997 *Electronic Transport in Mesoscopic Systems* (Cambridge: Cambridge University Press)
[30] LeVeque R J 2007 *Finite Difference Methods for Ordinary and Partial Differential Equations: Steady-State and Time-Dependent Problems* (Philadelphia: SIAM)